ELSEVIER

Journal of Magnetism and Magnetic Materials 151 (1995) 231–245

Journal of magnetism and magnetic materials

Wall structures in ferro/antiferromagnetic exchange-coupled bilayers: a numerical micromagnetic approach

M. Labrune *, J. Miltat

Laboratoire de Physique des Solides Université Paris-Sud and CNRS, F-91405 Orsay, France

Received 22 February 1995

Abstract

Two-dimensional wall structures in ferro/antiferromagnetically exchange-coupled bilayers are calculated by means of numerical micromagnetic simulations. Extended wall tails occurring in non-compensated structures are duly accounted for via the introduction of a variable meshing along one space direction. Constant charge finite volumes and the application of general boundary conditions in the presence of interlayer exchange coupling and/or surface anisotropy further characterize the computation scheme. Simulated wall structures in zero field are compared with various approximate analytical models and the ranges of validity of the latter are made explicit. Hard-axis field intrinsic magnetization and hysteresis properties are outlined, and a sketch of the wall structure phase diagram is proposed for given material parameters and a specific geometry.

1. Introduction

Due to the possible occurrence of a large perpendicular anisotropy and exceptional transport properties, magnetic multilayers are now well established candidates as potential media in information storage technology and field sensors. In both soft and hard ultrathin films, bilayers or multilayers, domain structures have been observed by means of electron transmission (DPC [1] and conventional Lorentz microscopy [2]), optical reflection or transmission (e.g. [3–8]) and spin-polarized secondary electrons (SEMPA, e.g. [9–11]). Wall structures in ultrathin films and multilayers are expected to differ markedly from the wall structures to be found in conventional thin films due to a new balance between the various energy terms. For instance, coupled Néel walls are preferred to uncoupled walls in a bilayer due to an efficient charge compensation [12]; similarly, superimposed Néel walls may, under the action of an in-plane hard-axis field, be transformed into complex structures made, in each layer, of a Néel wall plus a quasi-wall [5,13]. Two other physical properties of artificial magnetic stacks may influence wall profiles, namely, the possible existence of an interlayer exchange coupling and, as already stated, of a surface and/or interface anisotropy. According to the nature and thickness of the interlayer spacer, the former [4,14,15] may prove to be ferromagnetic (F) or antiferromagnetic (AF), or even biquadratic. The latter may become particularly strong in the case of very thin constitutive magnetic layers (e.g. [16,17]).

* Corresponding author. Fax: +33 1 69 41 60 86; email: labrune@lps.u-psud.fr.

SSDI 0304-8853(95)00328-2

The first aim of this paper is to offer a means of numerically simulating from first principles the wall structures in bilayers or multilayers within the micromagnetic approximation (Section 2). Interlayer exchange coupling and/or surface anisotropy are taken due account of, and the role of the new surface constraints deriving from those specific properties are emphasized. Selected examples of wall structures in symmetric bilayers as a function of the interlayer exchange coupling strength are given and discussed both in the F (Section 3) and the AF (Section 4) coupling regimes. Finally, Section 5 is devoted to intrinsic hysteretic properties of coupled walls in bilayers under the action of a hard-axis in-plane applied field.

2. Numerical

The code used in the present calculations minimizes the torque associated with the effective field $\boldsymbol{H}_{\text{eff}}$ acting on the magnetization $\boldsymbol{m} = \boldsymbol{M}/M_s$ ($\boldsymbol{m} = (\alpha,\beta,\gamma)$, $|\boldsymbol{m}| = 1$). The effective field defined as minus the derivative of the total energy with respect to $\boldsymbol{m}$, namely, $\boldsymbol{H}_{\text{eff}}(\boldsymbol{r}) = -\partial E_T/\partial \boldsymbol{m}$ comprises contributions from exchange, anisotropy, applied and demagnetizing field energies. At equilibrium, the equation

$$\boldsymbol{m} \times \boldsymbol{H}_{\text{eff}} = \boldsymbol{0} \tag{1}$$

should be satisfied at all mesh points within the magnetic volume. In this respect, the present computations follow the original LaBonte–Brown scheme [18]. Compared with the codes initially developed [19,20], however, three main modifications have been introduced. The first concerns the incorporation of new surface constraints due to the existence of interlayer exchange coupling and/or of surface anisotropy. The second involves a new discretization scheme introducing a variable meshing along one space direction for a proper description of the well known logarithmic tails of Néel walls [21] or, more generally, the extended tails of uncompensated structures. A first account of the method was given in Ref. [22] and its application to Néel walls in very thin films was discussed in Ref. [23]. Finally, a bilinear variation of the magnetization distribution within each cell is assumed [24].

2.1. Surface constraints

Along the outer surfaces of the magnetic stack and in the absence of surface anisotropy, the magnetization should be stationary [25], a condition that reads

$$\partial \boldsymbol{m}/\partial \boldsymbol{n} = 0, \tag{2}$$

where $\boldsymbol{n}$ is a unit vector normal to the surface (OY axis). Eq. (2) would also apply to inner surfaces in the case of sole magnetostatic coupling. The set of equations (1) and (2) is usually referred to as the Brown micromagnetic equations [26].

More generally, however, the boundary conditions should be modified in the presence of:

(i) an interlayer exchange coupling, amplitudes J_1 and J_2, and energy density per unit surface:

$$\varepsilon_J(x) = J_1[1 - \boldsymbol{m}\cdot\boldsymbol{m}'] + J_2[1 - (\boldsymbol{m}\cdot\boldsymbol{m}')^2], \tag{3}$$

$\boldsymbol{m}$ and $\boldsymbol{m}'$ being magnetization vectors at the inner surfaces of the bilayer stack just facing each other (see Fig. 1). According to the usual definition, when $J_2 = 0$ or $|J_2| \ll |J_1|$, $J_1 > 0$ and $J_1 < 0$ mean a ferromagnetic (F) and antiferromagnetic (AF) exchange coupling, respectively. When $J_1 \approx 0$, a negative J_2 value leads to a biquadratic interlayer ex-

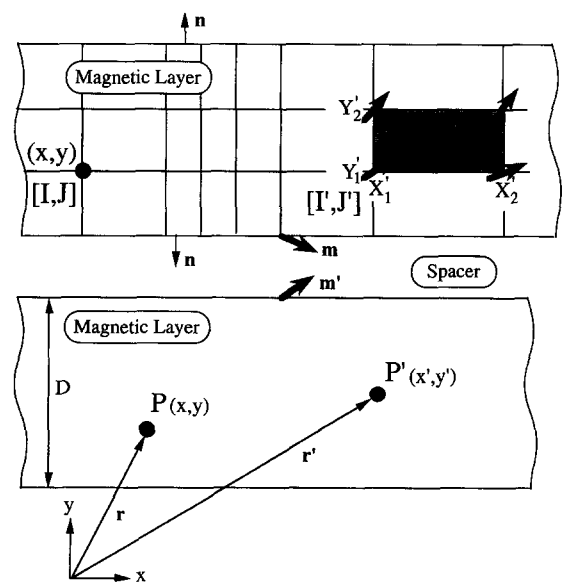

Fig. 1. Bilayer geometry, including a schematic representation of the variable meshing along the OX space direction.

change coupling type [4]. Owing to the above definition, a sole exchange interlayer coupling of the surface spins has been considered in the present simulations: the model reduces interactions to closest distance spins belonging to different and perfectly flat interfaces. Therefore, the interlayer exchange coupling contribution to the full energy only requires a single integration over X, where the OX axis is taken to be perpendicular to the wall elongation direction.

(ii) A surface anisotropy along the normal to the layers K_s with surface energy density

$$\varepsilon_K(x) = K_s\left[1 - (\boldsymbol{n}.\boldsymbol{m})^2\right]. \tag{4}$$

This last term should be integrated over X and the four surfaces ($i = 1,...,4$) of the bilayer stack, with potentially different magnitudes of the coefficient K_s for the various interfaces between the magnetic material and a non-magnetic spacer or vacuum.

Minimizing the total free energy through variational calculus yields the Euler equations in the volume and along surfaces (see e.g. Ref. [27]). The volume equation is identical to Eq. (1), whereas the surface equation, now including not only the bulk exchange contribution (constant A) but also the surface anisotropy and the interlayer exchange coupling, reads

$$2A\boldsymbol{m} \times \left(\frac{\partial \boldsymbol{m}}{\partial \boldsymbol{n}}\right) - 2K_s(\boldsymbol{n}.\boldsymbol{m})(\boldsymbol{m} \times \boldsymbol{n}) - J_1(\boldsymbol{m} \times \boldsymbol{m}') - 2J_2(\boldsymbol{m}.\boldsymbol{m}')(\boldsymbol{m} \times \boldsymbol{m}') = 0, \tag{5}$$

where the first contribution leads to Eq.(2) in the absence of surface anisotropy and interlayer exchange, while the existence of the two first contributions (A and K_s) gives rise to the Rado–Weertman relation [28] in the absence of interlayer exchange coupling. In the general case, the explicit new surface boundary condition reads

$$\frac{\partial \boldsymbol{m}}{\partial \boldsymbol{n}} = -\frac{J_1}{2A}\left[(\boldsymbol{m}\cdot\boldsymbol{m}')\boldsymbol{m} - \boldsymbol{m}'\right] + \frac{K_s}{A}(\boldsymbol{n}\cdot\boldsymbol{m})\left[\boldsymbol{n} - (\boldsymbol{n}\cdot\boldsymbol{m})\boldsymbol{m}\right] + \frac{J_2}{A}(\boldsymbol{m}\cdot\boldsymbol{m}')\left[\boldsymbol{m}' - (\boldsymbol{m}\cdot\boldsymbol{m}')\boldsymbol{m}\right]. \tag{6}$$

2.2. Discretization

The continuous magnetization distribution $\boldsymbol{m}(\boldsymbol{r})$ in the magnetic body is reduced to a finite number of magnetization vectors $\boldsymbol{m}(\boldsymbol{r}_i)$, with $i = 1,...,N$, where N is the total number of nodes. Evaluating the non-local magnetostatic term requires the knowledge of difference vectors $(\boldsymbol{r}_i - \boldsymbol{r}_{i'})$. Therefore, a periodic Cartesian grid is usually preferred since, due to the translational lattice invariance, one parameter only, namely $(i - i')$, suffices to characterize long-range force interactions between cells i and i'. In other words, the translational invariance reduces the size of the dipolar interaction coefficient matrices from $C_{VS}(i,i')$ to $C_{VS}(i - i')$, hence reducing memory requirements.

Unfortunately, the physical problems treated below incorporate uncompensated structures such as parallel Néel walls with two characteristic lengths [21,29] of markedly different magnitudes. The shortest of these lengths describes the wall core width to be characterized by a rapid variation of $\boldsymbol{m}$ scaling with $\delta_1 \approx \sqrt{A/2\pi M_s^2}$. The second characteristic length $\delta_2 \approx D/Q$, where D is the thickness of an individual layer and Q is the usual quality factor, corresponds to the extended Néel wall tail width ($Q = K/2\pi M_s^2$, where K is the bulk anisotropy constant; $Q \ll 1$ in the case of soft magnetic layers). The condition $\delta_2 \gg \delta_1$ applies in the cases considered below. Therefore a fair description of both parts of the wall based on a periodic grid would require an extremely large number of nodes N, which in turn would prove unacceptable in terms of computation time.

In the following, therefore, an adjustable meshing has been introduced along the X direction, as depicted schematically in Fig. 1, keeping in mind that the choice of a non-periodic grid leads to an increase in the size of the C_{VS} interaction coefficient matrices. It should be mentioned that a variable meshing along the sample normal (OY in the present geometry) was introduced in Ref. [30] for a proper description of the internal structure of 180° walls in thick iron layers.

Demagnetizing field

Following recent developments [24,31], the present calculations use a scheme assuming constant magnetic volume charges within one cell and con-

stant magnetic surface charges per cell boundary at the free surfaces or interfaces. In addition to an improvement in accuracy compared with the classical approach, assuming a constant magnetization within each discretization cell, mesh points are naturally introduced along the interfaces and/or surfaces of the stack; this is a necessary condition for a proper description of surface constraints as emphasized above (Section 2.1).

In the present work, the demagnetizing field contribution to $\boldsymbol{H}_{\text{eff}}$ in Eq. (1) is directly evaluated, knowing the distribution of volume, ρ, and surface charges, σ. Specializing to magnetization distributions invariant along one space direction, OZ in the present geometry, the continuous expression for the demagnetizing field at location $\boldsymbol{r}$ reads (see Fig. 1)

$$\boldsymbol{H}_{\text{d}}(\boldsymbol{r}) = 2\int\int \rho(\boldsymbol{r}')\frac{\boldsymbol{r}-\boldsymbol{r}'}{|\boldsymbol{r}-\boldsymbol{r}'|^2}\,\mathrm{d}x'\,\mathrm{d}y' + 2\int\int \sigma(\boldsymbol{r}')\frac{\boldsymbol{r}-\boldsymbol{r}'}{|\boldsymbol{r}-\boldsymbol{r}'|^2}\,\mathrm{d}x', \tag{7}$$

where $\boldsymbol{r} = \boldsymbol{r}(x,y)$, $\sigma = M_{\text{s}}(\boldsymbol{m}\cdot\boldsymbol{n})$, and

$$\rho = -M_{\text{s}}\,\mathrm{div}(\boldsymbol{m}) = -M_{\text{s}}\left(\frac{\partial\alpha}{\partial x}+\frac{\partial\beta}{\partial y}\right).$$

For each layer, the normal $\boldsymbol{n}$ points outwards, hence $\sigma = \pm M_{\text{s}}\beta$. Assuming a regular meshing along the y-direction, the discretized equivalent to the volume contribution of the x-component of the demagnetizing field in Eq. (7) reads

$$H^{\text{vol}}_{\text{d}x}(I,J) = \sum_{I'}\sum_{J'}\rho(I',J')C^{x}_{\text{vol}}(I,I',J'-J), \tag{8}$$

where

$$C^{x}_{\text{vol}}(I,I',J'-J) = 2\int_{x'_1}^{x'_2}\int_{y'_1}^{y'_2}\frac{x-x'}{(x-x')^2+(y-y')^2}\,\mathrm{d}x'\,\mathrm{d}y',$$

$$x = x(I), \qquad y = y(J),$$

$$x'_1 = x'(I'), \qquad y'_1 = y'(J'),$$

$$x'_2 = x'(I'+1), \qquad y'_2 = y'(J'+1),$$

$$\rho(I',J') = -M_{\text{s}}\langle\mathrm{div}(\boldsymbol{m})\rangle_{I',J'}.$$

In the case of a bilinear variation of the magnetization within each cell, the average volumic charge is expressed as (divergence theorem)

$$\langle\mathrm{div}(\boldsymbol{m})\rangle_{kl} = \frac{1}{2[x(l+1)-x(l)]}\big(\alpha(k+1,l+1) + \alpha(k+1,l) - \alpha(k,l+1) - \alpha(k,l)\big) + \frac{1}{2[y(k+1)-y(k)]}\big(\beta(k+1,l+1) + \beta(k,l+1) - \beta(k+1,l) - \beta(k,l)\big). \tag{9}$$

Equivalent expressions hold for the y-component of the demagnetizing field arising from volume charges. Contributions from surface charges may be evaluated in a similar fashion.

Finally, the stray field energy E_{d} is calculated using the classical continuous expression (Eq. 10), assuming, within each cell, a bilinear variation of both the magnetization and the demagnetizing field:

$$E_{\text{d}} = -\frac{1}{2}\int_{V}\boldsymbol{H}_{\text{d}}\cdot\boldsymbol{M}\,\mathrm{d}V. \tag{10}$$

Exchange interactions

The bulk exchange contribution to the effective field involves the computation of the second derivatives of the magnetization components versus space coordinates. Since a four-nearest-neighbour approximation has, in the case of regular meshings [19], been found to be far superior to the conventional two-nearest-neighbour definition in terms of numerical precision, the same approach is followed below. Considering five mesh points located at coordinates $x_{i-2}\ldots x_{i+2}$ (see Fig. 2), Taylor expansion to the fourth order around the central mesh point provides a set of four linear equations in increasing order of the derivatives, f', f'', f''', f^{iv} of the function f, namely,

$$(x_{i+m}-x_i)f'(x_i) + \frac{(x_{i+m}-x_i)^2}{2!}f''(x_i) + \frac{(x_{i+m}-x_i)^3}{3!}f'''(x_i) + \frac{(x_{i+m}-x_i)^4}{4!}f^{\text{iv}}(x_i) = f(x_{i+m})-f(x_i), \qquad m=-2,+2,\ m\neq i. \tag{11}$$

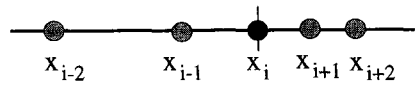

Fig. 2. Four-nearest-neighbour approximation as used in the evaluation of bulk exchange interactions.

Solving this system for the second-order derivative f'' provides the sought-for answer. The solution for an arbitrary meshing reduces to the expression previously utilized [19] when the distance between mesh points becomes constant.

Implementation of boundary conditions

Proper boundary conditions are simply inserted as a particular treatment of the exchange interactions when the mesh points are located either along one of the free surfaces or interfaces, or one mesh constant away from the former.

When the mesh point is located along free surfaces or interfaces, Taylor expansion around y_j (see Fig. 3, right column) yields a set of three linear equations in the variables f'', f''' and f^{iv}, duly incorporating boundary conditions $f'(y_j)$, namely,

$$\frac{(y_{j-n}-y_j)^2}{2!}f''(y_j)+\frac{(y_{j-n}-y_j)^3}{3!}f'''(y_j)+\frac{(y_{j-n}-y_j)^4}{4!}f^{iv}(y_j)=f(y_{j-n})-f(y_j)-(y_{j-n}-y_j)f'(y_j),\quad n=1,3. \tag{12}$$

Similarly, for mesh points one mesh constant away from free surfaces or interfaces (Fig. 3, left column),

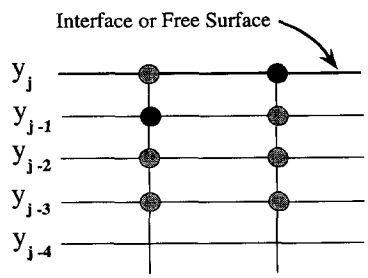

Fig. 3. Geometry specific to mesh points located close to a free surface or an interface (see text for details).

expansion around y_{j-1} followed by an evaluation of the first derivative at y_j provides the first equation:

$$f'(y_{j-1})+(y_j-y_{j-1})f''(y_{j-1})+\frac{(y_j-y_{j-1})^2}{2!}f'''(y_{j-1})+\frac{(y_j-y_{j-1})^3}{3!}f^{iv}(y_{j-1})=f'(y_j). \tag{13a}$$

The three other equations are just equivalent to the general equations (11), precisely:

$$(y_{j-n}-y_{j-1})f'(y_{j-1})+\frac{(y_{j-n}-y_{j-1})^2}{2!}f''(y_{j-1})+\frac{(y_{j-n}-y_{j-1})^3}{3!}f'''(y_{j-1})+\frac{(y_{j-n}-y_{j-1})^4}{4!}f^{iv}(y_{j-1})=f(y_{j-n})-f(y_{j-1}),\quad n=0,+3,\ n\neq j-1. \tag{13b}$$

Thus, for those mesh points, similarly to the general case, a set of four linear equations in the variables f', f'', f''' and f^{iv} provide the value of the required second derivative. Because it includes the boundary condition, one equation plays a particular role.

3. Wall structures in the ferromagnetic exchange coupling regime

In the case of a ferromagnetic type interlayer exchange coupling two structures may be envisaged. One is composed of superimposed walls with opposite core magnetizations [32], thus drastically reducing the stray field energy (Fig. 4b). For large values of J, however, a second configuration made of parallel Néel walls (Fig. 4c) is expected to be energetically more stable. This section is primarily devoted to a description of superimposed walls in zero field. All calculations assume magnetic parameters typical of standard permalloy films (uniaxial in plane volume anisotropy: $K = 10^3$ erg/cm^3; volume exchange constant $A = 10^{-6}$ erg/cm, saturation magnetization $M_s = 800$ emu/cm^3). In Section 3.1 a single geometry is considered, namely, a bilayer with

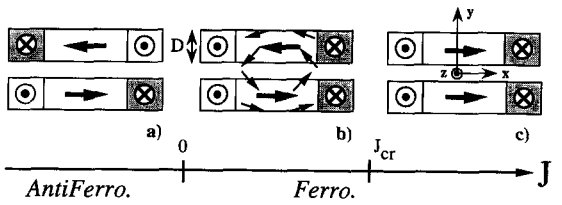

Fig. 4. Schematic diagram of superimposed 180° walls in a bilayer: (a) antiferromagnetic interlayer exchange coupling ($J < 0$); (b) ferromagnetic exchange coupling ($J > 0$); and (c) parallel Néel walls expected for larger J values.

magnetic layers $D = 8$ nm thick separated by a non-magnetic spacer, thickness $d = 2$ nm. Wall profiles are analyzed as a function of J ($J_2 = 0$, $J \equiv J_1$). In Section 3.2, the results obtained as a function of D and J are compared with previously published data [5,12]. The section ends with a consideration of the relative stability of these two structures versus J.

3.1. Superimposed walls in zero field

The calculation starts from an initial and arbitrary structure assumed, however, to be compatible with the superimposed wall structure of Fig. 4(b). As long as J keeps a moderate value, the equilibrium structure obtained in zero field is also composed of superimposed walls. Fig. 5 and Fig. 6 provide illustrations of the wall profile in one layer of the stack.

Fig. 5(a) shows the variation in $\boldsymbol{m}_x$ measured at the interface level versus distance from the core of the wall. In order to emphasize the potential occurrence of far-reaching wall tails, all wall profiles are plotted using a logarithmic scale. An increase in the ferromagnetic exchange coupling J significantly reduces the width W of the wall corresponding to regions where the magnetizations in adjacent layers have strong antiparallel components, in agreement with experimental data [33]. As explained below, for large values of J, the $\boldsymbol{m}_z$ component may be expressed as $\boldsymbol{m}_z \approx \tanh(X/\lambda)$, where $\lambda \approx \sqrt{A/K_{\text{eff}}}$. The effective anisotropy $K_{\text{eff}} = K + J/D$, K being the uniaxial bulk anisotropy constant. The wall width then amounts to $W = 2\lambda$.

The two-dimensional character of the present computations allows for a precise determination of the variation of the magnetization across the thickness of each layer. The wall width proves to be depth (Y) dependent, being slightly larger at the free surfaces of the magnetic stack than at interfaces. Besides, a quantitative analysis of the flux closure between the magnetic layers as schematically depicted in Fig. 4(b) may be performed. Results are summarized in Fig. 5(b), where the normal magnetization component at the interface is plotted versus X, with J as a parameter. As expected, the amount of flux closure remains moderate, the largest deviation angle not exceeding some 8° for the largest J considered. Furthermore, the variation of $\boldsymbol{m}_y$ may also be followed throughout the stack at a given distance X from the wall core (Fig. 6). This last curve is also an illustration of the general boundary conditions expressed by Eq. (6). In the vicinity of the

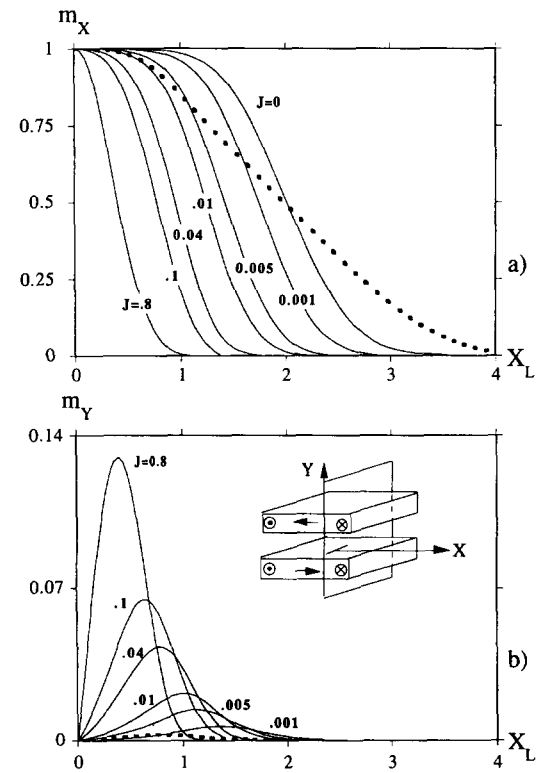

Fig. 5. Compensated 180° wall profiles versus X_L at interface level with the interlayer exchange constant J (erg/cm^2) as a parameter. X_L is a measure of the distance to the wall core ($x = 0$) owing to a log scale defined as: $X_L = (x/|x|)\log_{10}[1 + (|x|/D)]$. (a) m_x magnetization component; (b) m_y (notice the dilated scale). Permalloy (NiFe) material parameters. [8/2/8] nm bilayer geometry. The dashed line represents a Néel wall profile in a single NiFe film, 8 nm thick.

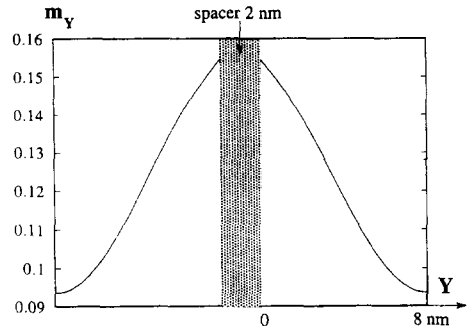

Fig. 6. Variation of the normal component m_Y versus Y across the bilayer at the x position corresponding to the maximum m_Y amplitude in Fig. 5(b), $J = 0.8$ erg/cm^2.

outer surfaces and in the absence of surface anisotropy, the magnetization is clearly stationary as anticipated by Eq. (6), here reducing to Eq. (2). Along the inner surfaces, however, the non-zero slope of the profile is a clear indication of the presence of an interlayer exchange coupling.

3.2. Energy considerations

A model of the magnetization distribution in bilayers was first proposed by Slonczewski [12,32]. The hypotheses intrinsic to this model are the following: (i) no exchange coupling between the magnetic layers ($J = 0$). The $\boldsymbol{m}_x$ component is assumed to be (ii) a sole function of x and varies slowly on a scale measured by D. Furthermore, each magnetic layer must satisfy (iii) div($\boldsymbol{m}$) = 0, all the magnetic charges being gathered at the interfaces, opposite charges facing each other. Finally, (iv) the classical bulk exchange contribution is neglected ($A = 0$). Owing to these assumptions, the wall structure is governed by an equilibrium between the stray field energy mainly concentrated in the non-magnetic spacer and the anisotropy energy in the magnetic layers. This model was later improved to include bulk exchange ($A \neq 0$) and applied to the particular case of the so-called edge-curling walls [34]. Superimposed Néel walls, now including interlayer exchange coupling, could be treated on the same footing [33]. A parametrized (Ritz) extension of these analytical models, including both exchange coupling ($J \neq 0$) and a more comprehensive treatment of demagnetizing field effects, has also been developed in order to determine to a good degree of accuracy 180° wall profiles in bilayers [5].

In the case of very thin magnetic layers, the validity of assumption (iii) appears questionable. The present 2D model makes assumption neither on the shape of the wall nor on the location of the magnetic charges. Therefore, ranges of validity of given approximations may be evaluated.

Looking throughout the lower magnetic layer in the region of positive X (Fig. 4b), the total amount of magnetic charges over a volume with length L along the wall elongation direction (Z-axis) is, in view of the (Gauss) divergence theorem, equal to

$$\iiint \rho \, dV + \iint \sigma \, dS = +M_s DL, \tag{14}$$

where ρ and σ are the magnetic volume and surface charge densities, respectively. Therefore, in units of $(M_s DL)^{-1}$, the following identity may written:

$$q_V + q_{iS} + q_{oS} = +1, \tag{15}$$

where q_V is the volume charge, the two other terms being the surface charges at the inner (iS) and outer (oS) surfaces of the magnetic layer, respectively. Within the given set of parameters and geometry used the total magnetic volume charge is found to be equal to $q_V \approx 0.818$ for $J = 0.8$ erg/cm^2 and proves rather insensitive to J in the range 0.1–0.8 erg/cm^2. At the same time, q_{oS} and q_{iS} amount to ~ -0.307 and $\sim +0.489$ for $J = 0.8$ erg/cm^2, respectively. Both integrated surface charges slightly increase in absolute value with decreasing J. It must be kept in mind, however, that an increase of J implies a drastic reduction of the area over which these charges are spread. Altogether, these results show that, charges are not solely located in the immediate vicinity of the inner surfaces of the stack. The reduction of the stray field problem to that of a parallel-plane capacitor therefore hardly appears justified.

In order to illustrate this problem, let us attempt to answer the following rather academic question: how is the charge distribution in the magnetic stack affected when, for a given thickness of the non-magnetic spacer and a constant exchange coupling, the thickness of each magnetic layer increases?. Results are gathered in Fig. 7. For all values of D, relation (15) is fulfilled due to the symmetry of the problem with respect of the OX and OY axes (i.e. all equilibrium profiles are such that $\boldsymbol{m}_x = 1$ or -1 at $x = 0$ in

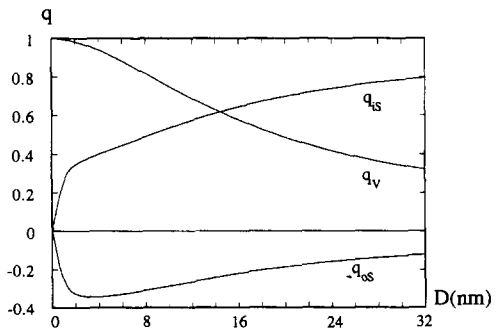

Fig. 7. Variation of the total amount of magnetic charges (reduced units) versus the thickness D of each magnetic layer, within the $X \geq 0$ volume of a single layer. q_v denotes volume charges, q_{iS} the surface charges at the interface, and q_{oS} the surface charges at the free surface. $[D/2\ \text{nm}/D]$ bilayer geometry, NiFe, $J = 0.8$ erg/cm^2.

both layers). When the thickness of each magnetic layer vanishes, no surface charges are expected. Increasing the thickness of each film leads to a decrease of in q_V. Simultaneously, charges of opposite sign appear on the opposite surfaces of each magnetic layer, always fulfilling the inequality $q_{iS} > |q_{oS}|$. This observation is the signature of a ripening of the interlayer magnetostatic coupling. For large values of D, q_V still decreases towards zero, now together with $|q_{oS}|$. Conversely, q_{iS} tends towards unity. Stated differently, all the magnetic charges are gathered at the inner surfaces, thus delimiting the range of validity of Slonczewski's model.

The corresponding variations in wall energy are plotted in Fig. 8(a–c) and are compared with the results of a model due to Tomáš et al. [5], as well as with the $4\sqrt{AK_{\text{eff}}}$ approximation. This last approximation may be obtained through the following crude model. Let us assume first that the stray field contribution is vanishingly small; second, that $\boldsymbol{m}$ always belongs to the plane of the films; while, third, that ϕ, the angle between $\boldsymbol{m}$ and the easy axis is a sole function of x. Taking into account the superimposed wall symmetry, namely, $\phi_1(x) = -\phi_2(x) = \phi(x)$, where the subscripts 1 and 2 refer to the lower and upper layers, respectively, the total energy reads

$$E = \int\int\int \left[A\left(\frac{\partial\phi}{\partial x}\right)^2 + K\sin^2(\phi) \right] \mathrm{d}V + \int\int 2J\sin^2(\phi)\,\mathrm{d}S. \qquad (16)$$

Under the governing assumptions, a straightforward integration over the thickness of both magnetic layers yields

$$E = \int\int \left[2DA\left(\frac{\partial\phi}{\partial x}\right)^2 + 2DK\sin^2(\phi) + 2J\sin^2(\phi) \right] \mathrm{d}S,$$

or

$$E = 2D\int\int \left[A\left(\frac{\partial\phi}{\partial x}\right)^2 + K_{\text{eff}}\sin^2(\phi) \right] \mathrm{d}S. \qquad (17)$$

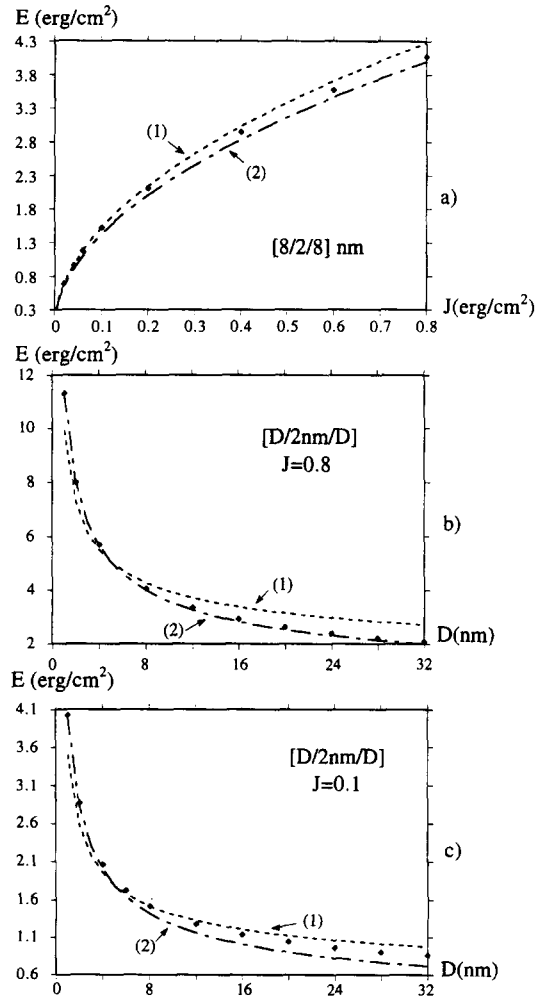

Fig. 8. Variation of the wall energy (a) versus J for a [8/2/8] nm NiFe bilayer geometry; (b,c) versus D for a $[D/2\ \text{nm}/D]$ bilayer geometry. $J = 0.8$ erg/cm^2 (b), $J = 0.1$ erg/cm^2 (c). Full symbols correspond to computed values; curve 1 refers to the model of Ref. [7], and curve 2 to the $E = \sqrt{AK_{\text{eff}}}$ approximation (see text for details).

Due to the exact analogy with the energy of a pure Bloch wall, the following relationships are obtained at once:

$$E = 4\sqrt{AK_{\text{eff}}} \quad \text{with} \quad E_A = E_{K_{\text{eff}}} = E/2,$$

$$m_Z = \cos(\phi) = \tanh(x/\lambda). \tag{18}$$

In Fig. 8(a), for a given layer thickness $D = 8$ nm, it is observed that Tomáš' Ritz model (curve 1) is in rather good agreement with our numerical calculations for moderate J values. On the other hand, if J increases beyond, say, 0.4 erg/cm^2, the 'crude' model excluding charges altogether becomes better. In this last situation the interlayer exchange coupling dominates the dipolar coupling and the set of relations (18) are in agreement with all features described in Section 3.1. Now, for thin layers and for a large range of J values (see Fig. 8b,c), the same conclusions may be drawn. This time the $1/D$ contribution in the effective anisotropy plays the leading role.

3.3. Equilibrium structure

In zero applied field, energy considerations show that parallel Néel walls are favoured for J values higher than $J_{c1} = 0.08$ erg/cm^2. However, from the very beginning of each micromagnetic calculation, one must choose an initial and arbitrary structure. If it is already compatible with the superimposed wall structure of Fig. 4(b), the equilibrium wall configuration is usually a superimposed structure too, a configuration obviously locked into a local energy minimum when $J > J_{c1}$. An energy barrier associated to a quasi-topological transition must be overcome before parallel Néel walls can be nucleated [35]. Indeed, a continuous transition implies that one of the walls be temporally transformed into a Bloch type wall, an energetically extremely costly transition. Such a mechanism is only found to occur for $J > J_{c2} = 0.86$ erg/cm^2 for the geometry considered.

4. Wall structures in the antiferromagnetic exchange coupling regime

For an antiferromagnetic interlayer exchange coupling ($J < 0$), and in the absence of applied field, a single wall structure is expected (Fig. 4a) since the magnetization distribution is stabilized both by interlayer exchange and magnetostatic coupling. The wall structure symmetry reads $m_Z(x,y_1) = -m_Z(x,y_2)$ instead of $m_Z(x,y_1) = +m_Z(x,y_2)$ in the ferromagnetic coupling case, as illustrated in Fig. 9. The variation of J, as long as $J \leq 0$, has little effect on the equilibrium wall profile. In all cases the m_Y component proves rather small and decreases with decreasing J. Disregarding this component, equilibrium structures are characterized by a perfect antiparallel alignment of the magnetizations, namely $m_1 = -m_2$ in spite of the fact that no symmetry was intentionally introduced in the code.

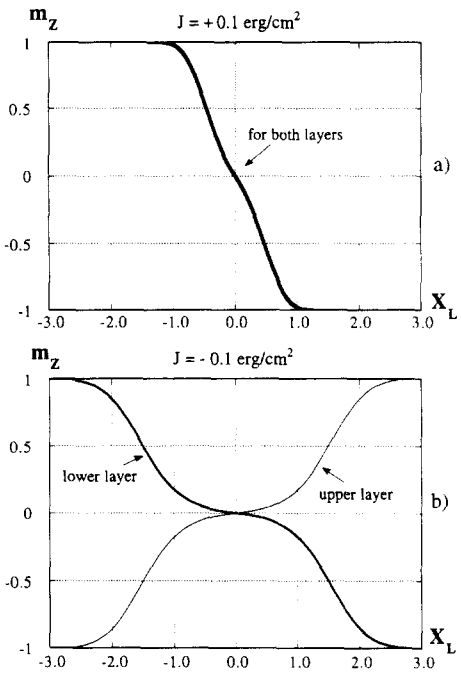

Fig. 9. Wall profile (longitudinal magnetization component m_Z versus X_L), emphasizing the different symmetries relating to (a) ferromagnetic interlayer exchange coupling, (b) antiferromagnetic coupling. [8/2/8] nm NiFe bilayer geometry.

Because of the local charge compensation, wall profiles in a symmetric bilayer satisfying $J < 0$ are expected to be narrower than a Néel wall in a single layer with thickness equal to that of a single layer of the stack, and wider than a Bloch wall totally deprived of magnetostatic interactions. Simulations confirm this simple argument (Fig. 10).

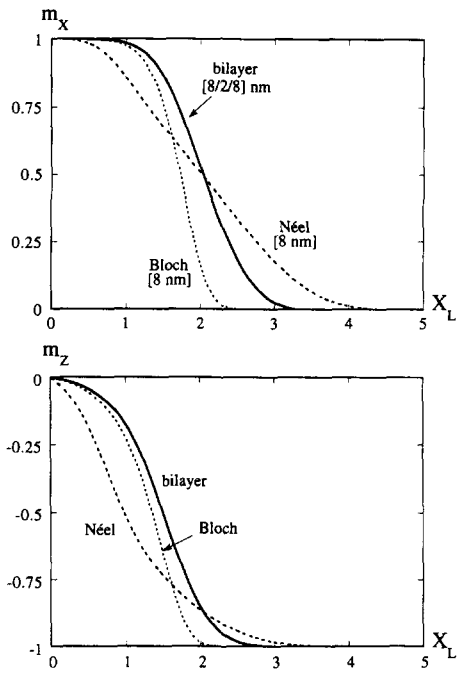

Fig. 10. Comparison of (a) transverse m_X and (b) longitudinal m_Z magnetization components in 180° walls including a Néel and a pure Bloch wall in a single NiFe film, 8 nm thick, and a compensated wall in a NiFe [8/2/8] nm symmetric bilayer with antiferromagnetic interlayer exchange coupling ($J = -0.1$ erg/cm^2).

Compared with the ferromagnetic coupling case, where the exchange coupling energy plays a leading role in the total energy balance, the exchange coupling energy density proves roughly constant when

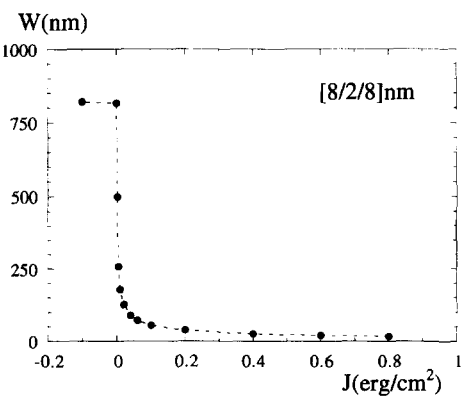

Fig. 11. Compensated 180° wall width versus J in a NiFe [8/2/8] nm bilayer.

$J < 0$ and independent of x. Therefore, only a slight decrease in the wall width W, defined as

$$W = 2/(\partial m_Z/\partial x)_{x=0}, \tag{19}$$

is observed in the antiferromagnetic coupling regime as a function of increasing J. When entering the ferromagnetic coupling regime, the wall width falls abruptly asymptotically following a $W \approx 2\sqrt{A/K_{\text{eff}}}$ law for large J values, as indicated in Section 3. Computational results are summarized in Fig. 11.

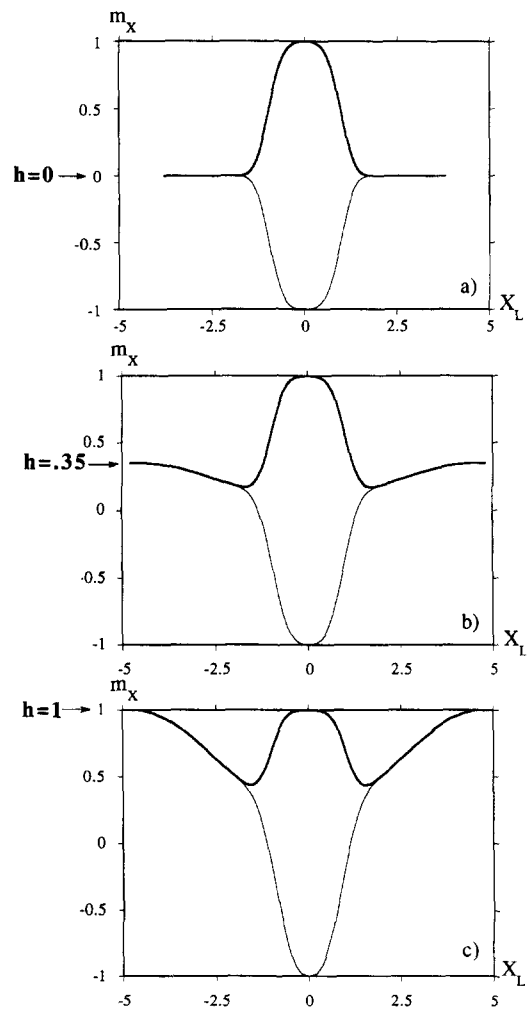

Fig. 12. Variation of the m_X magnetization component versus X_L at interface level across the upper and lower layer walls as a function of an hard axis field (reduced units) (a) $h = 0$, (b) $h = 0.35$, and (c) $h = 1$. Note the presence of logarithmic tails in (b) and (c). Weak ferromagnetic-type interlayer exchange coupling: $J = 0.04$ erg/cm^2. NiFe [8/2/8] nm bilayer geometry.

5. Wall structures as a function of a hard-axis field

In a first step the virgin curve, i.e. the evolution of the wall pattern versus hard-axis field, is described in Section 5.1, each simulation starting from the equilibrium superimposed wall structure obtained when $H = 0$. In a second step the full hysteresis loop is considered in Section 5.2. The initial structure now corresponds to a saturated state. Intermediate wall structures include parallel Néel walls ($J \gg 0$), as well as walls + quasi-walls for low $J > 0$ values, and similar although more pronounced structures for $J < 0$.

5.1. Virgin curve: ferromagnetic coupling

The calculation proceeds from the equilibrium superimposed wall structure described in Section 3.1. Under the action of an external field applied along

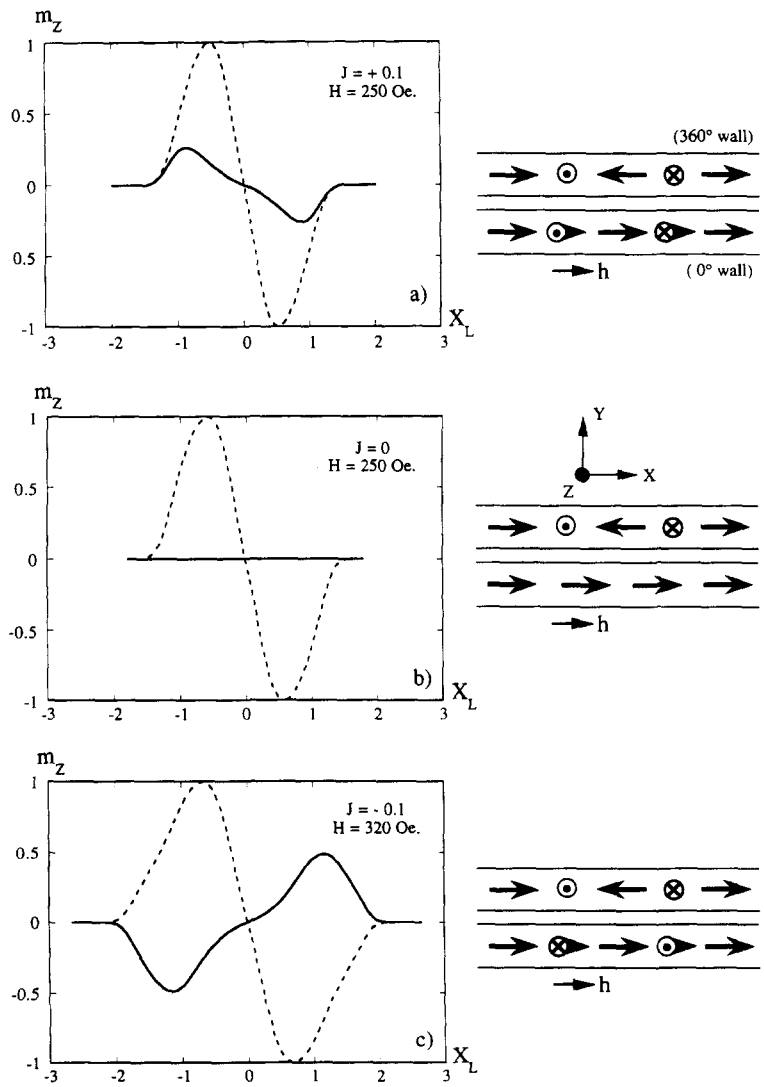

Fig. 13. Variation of the m_z magnetization component at interface level in the upper (dashed lines) and lower (continuous lines) layers of a NiFe [8/2/8] nm bilayer under the application of a strong hard-axis field. (a) Ferromagnetic interlayer exchange coupling, (b) no exchange coupling, and (c) antiferromagnetic coupling. Schematic wall and quasi-wall configurations are shown on the right.

$+OX$ (in-plane hard axis) the magnetization inside each domain of the constitutive layers, initially oriented along OZ ($m_X = 0$; $m_Z = \pm 1$), is assumed to rotate freely towards the field direction according to the Stoner–Wohlfarth model [36], namely, $m_X = +h$, $m_Z = \pm(1-h^2)^{1/2}$ with $h = H/H_K$, where H_K is the usual anisotropy field $2K/M_s$.

As soon as the field is applied, the overall magnetic structure of the stack becomes uncompensated. For the positive X part of the bilayer the total charge (in reduced units) varies as $-(1+h)$ in one of the layers (here the upper layer), and as $+(1-h)$ [$h \leq 1$] in the other. Charge non-compensation leads to a large increase in the wall width in the range $h \approx 0$–1. Walls are now characterized by the presence of logarithmic tails (Fig. 12) similar to the well known Néel wall tails in conventional thin films. Such a mechanism was already pointed out in Ref. [5].

For $h \geq 1$, a 360° wall is nucleated in, owing to the present convention, the upper layer. Its width decreases with increasing field. Simultaneously, the second layer becomes gradually saturated. A small oscillation of $\boldsymbol{M}$ towards the film normal is, however, still noticeable due to the strong demagnetizing field produced by the 360° wall. Moreover, a component also develops along OZ because of exchange coupling (compare Fig. 13a and b). It increases with increasing J (not shown).

As already stated, full saturation requires, within a 2D model, the formation of a transient Bloch wall. This is achieved in a field (H_c) substantially larger than H_K. The dependence of the critical field H_c on J is depicted in Fig. 14. In fact, the energy barrier for such a transition is mainly governed by the demagnetizing energy which may be extremely large in soft materials leading to ultimately compressed magnetization distributions. It ensues that our simulated transition fields H_c are strongly mesh dependent although remaining intrinsic [35]. As a consequence, transition fields are known to only a limited precision. Experimentally, huge fields have been shown necessary for the erasure of a 360° wall in the case of a sole dipolar interlayer coupling (the $J = 0$ limit) [37]. It should be noticed, however, that, according to the same authors (see also Ref. [38]), the 360° wall assumes a zigzag shape as soon as the field exceeds H_K. The 2D aspect of the present computations can include neither such an effect nor the possible influence of Bloch lines which may efficiently assist the transition [39], in spite of a limited influence in very thin layers [40]. Therefore, care should be taken before applying the above results directly.

5.2. Virgin curve: antiferromagnetic coupling

Because the present calculations require fixed boundary conditions as $x \to \pm\infty$, a precise knowledge of the exact magnetization direction in adjacent domains, as a function of the applied field, is first required. Assuming in a first step a uniform magnetization in the domains, noticeably along the film normal, the following total energy has to be minimized:

$$E = 2KD\sin^2\phi + 2J(1-\sin^2\phi) - 2H_a M_s D\sin\phi, \qquad (20)$$

where $\phi = \phi_1 = \pi - \phi_2$, ϕ_1 and ϕ_2 are the angles between $\boldsymbol{M}$ and the easy axis in layers 1 and 2, respectively. Minimizing the energy yields the equilibrium angle:

$$m_x = \alpha = \sin\phi = H_a M_s / 2K_{\text{eff}}, \quad \text{where}$$
$$K_{\text{eff}} = K + |J|/D. \qquad (21)$$

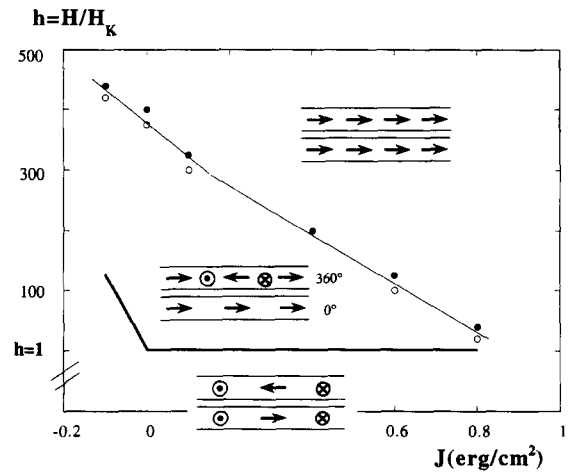

Fig. 14. Computed phase diagram in an increasing field assuming a superimposed wall initial state. The saturation field lies in between the field values corresponding to the last numerical simulation, still yielding a 360°/0° wall configuration (open symbols) and the first computed saturated state (full symbols). The thin transition line only serves as a guide for the eye. NiFe [8/2/8] nm bilayer geometry.

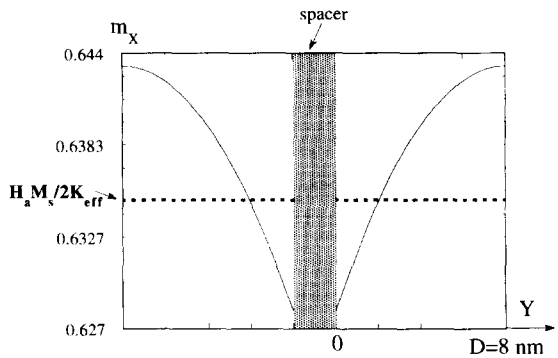

Fig. 15. Variation of the m_X magnetization component versus Y across the bilayer in the "domain region" (i.e. areas where $\boldsymbol{m}$ is a sole function of y) in the case of an antiferromagnetic interlayer exchange coupling. The dashed lines correspond to the assumption of a uniform $\boldsymbol{m}$. NiFe [8/2/8] nm bilayer geometry. $J = -0.1$ erg/cm^2, $h = 80$. Note the dilated vertical scale.

Relation (21) shows that the state of saturation is reached for a field much higher than the anisotropy field (e.g. $H_{sat} = 320$ Oe for $J = -0.1$ erg/cm^2, whereas $H_K = 2.5$ Oe). The field must indeed overcome both the anisotropy and the interlayer exchange coupling barriers before saturation may be reached.

However, assuming that the exchange coupling is active only at the interface level (the present model), the magnetization distribution need not be uniform through the thickness of each layer. Rather, a better alignment of $\boldsymbol{M}$ with the field direction should be reached when moving from the interfaces ($y = 0$) to the free surfaces ($y = D$). The following Euler equation needs to be fulfilled at interfaces:

$$\frac{J^2}{A}\alpha^2(0)\left[1-\alpha^2(0)\right] = H_aM_s\left[\alpha(D)-\alpha(0)\right] - K\left[\alpha^2(D)-\alpha^2(0)\right]. \tag{22}$$

As shown in the computed profile in Fig. 15, relation (21), i.e. $\alpha(D) = \alpha(0) = H_aM_s/2K_{eff}$, which is valid in the limit of an infinite bulk exchange stiffness A, only proves to be some kind of average value, the real profile taking due account of the boundary conditions (22) at interfaces and the usual $\partial\boldsymbol{m}/\partial\boldsymbol{n} = 0$ boundary conditions at free surfaces. Although weak due to the limited thickness of the layers, a torsion of the magnetization across the layers thickness is clearly identified. The calculation of wall profiles has thus been performed as follows: during the first 100 or so iteration loops, the magnetization vector $\boldsymbol{m}$ at both extremities of the computation zone in both layers is fixed and follows the relationship depicted by Eq. (21). The essential features of the sought-for wall configuration are gathered during these initial iteration loops. The above constraints are then relaxed, yielding, provided that the computation region is large enough, the proper depth-dependent magnetization profile within domains.

Results pertaining to antiferromagnetically coupled bilayers may be analyzed in the light of those obtained in the ferromagnetic exchange coupling regime. As soon as the hard-axis field exceeds $2K_{eff}/M_s$, a 360°/0° wall structure is also nucleated. The m_z component oscillation within the 0° wall is now compatible with the character of the exchange coupling (compare Fig. 13(c) and (a)). Besides, the transition field H_c is increased compared with the ferromagnetic situation and can be obtained by a simple extrapolation of the H_c curve in Fig. 14 into the $J < 0$ region.

5.3. Hysteresis curve

The initial structure of the bilayer is assumed saturated along, say, $+OX$. As long as $h \geq 1$ ($h \geq h_{sat} \approx [1 + |J|/KD]$) in the ferromagnetic (antiferromagnetic) coupling regime, this saturated state is preserved. Below those values, domain walls may be nucleated through the gradual rotation of the magnetization within domains, ending up, for $h = -1$ ($h = -h_{sat}$), with two superimposed 360° walls. For relatively large positive J values, the wall structure for $|h| \leq 1$ consists in two parallel Néel walls. As J decreases a different wall structure is found to nucleate, consisting in a wall plus a quasi-wall in each layer. Finally, in a large reverse field, full saturation along $-OX$ is achieved. For instance, the 360°/360° structure requires a field as high as $H = -60H_K$ to be destroyed when $J = +0.8$ erg/cm^2 for the geometry considered. It may be remarked that this field value amounts to roughly twice the corresponding critical field needed to erase a (360°/0°) configuration (Section 5.1.1). The computational results are summarized in Fig. 16. Schematic hysteresis cycles

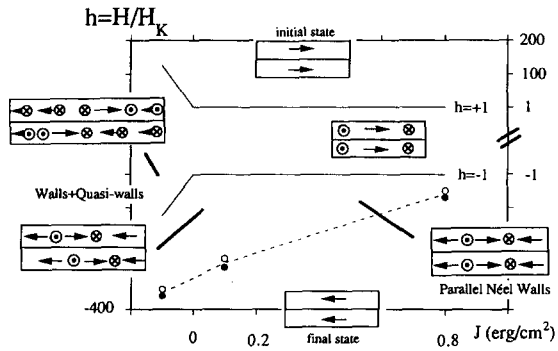

Fig. 16. Computed phase diagram in a decreasing field. Conventions identical to those in Fig. 14.

may now be completed by symmetry. It is seen that, in the limit of 2D magnetization distributions, extremely strong intrinsic hysteresis phenomena confined to wall regions do take place in exchange-coupled bilayers.

As indicated above, wall/quasi-wall structures occur either in a state of antiferromagnetic interlayer coupling or in a regime of weak ferromagnetic coupling. These structures arise from a better charge compensation (pseudo-quadrupolar distribution) when compared to pure superimposed Néel walls [13] and/or from exchange interactions when $J < 0$. Examples of wall/quasi-wall structures are exhibited in Fig. 17 ($J = +0.1$) and Fig. 18 ($J = -0.1$). It is noteworthy that, when $J < 0$, due to the initial saturation, wall structures may not be free from sections with parallel magnetizations. Due to exchange interactions, however, the real wall sections of each wall/quasi-wall pair are subjected to repulsive forces. For the same reason, the quasi-wall section soon becomes fully developed. Finally, it may also be noted that, contrary to the $J < 0$ regime, the nucleation of the wall/quasi-wall twin pattern occurs only for a negative H_x field when $J > 0$ in the range of thicknesses investigated (see also Ref. [5]).

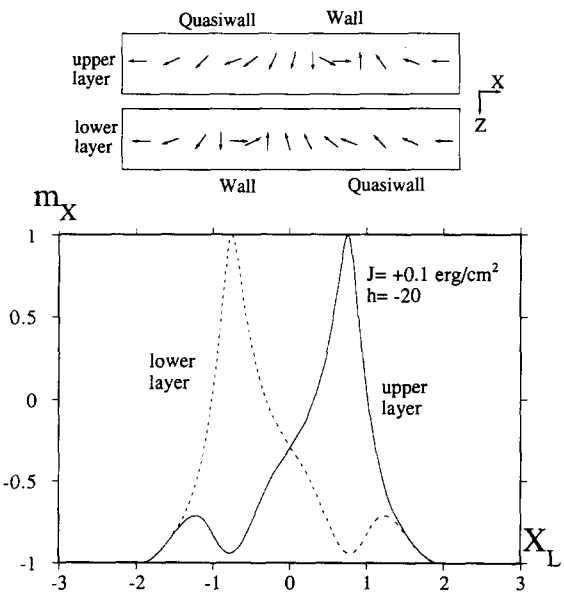

Fig. 17. Wall plus quasi-wall profiles observed in the case of moderate ferromagnetic coupling ($J = +0.1$ erg/cm^2) under the action of a reverse hard-axis field ($h = -20$). The inset shows the corresponding variations of $\boldsymbol{m}$ in the sample plane (XOZ) in the middle of the upper and lower magnetic layers, respectively. NiFe [8/2/8] nm bilayer geometry.

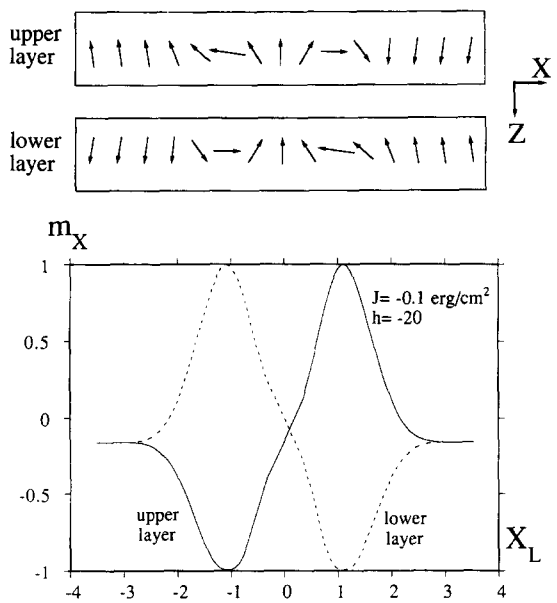

Fig. 18. As Fig. 17 in the case of antiferromagnetic interlayer exchange coupling ($J = -0.1$ erg/cm^2, $h = -20$).

6. Conclusions

Ab initio 2D numerical simulation of wall profiles in thin magnetic bilayers have been performed. Due to the introduction of an adjustable meshing, a fair description of the long-range tails usually encoun-

tered in uncompensated structures has been achieved. Wall structures to be found in ferromagnetic and antiferromagnetic exchange-coupled layers have been investigated and the general analytical solution for boundary conditions derived. The widths of superimposed wall structures in zero field has been shown to depend drastically on the magnitude of the interlayer exchange coupling constant in the $J > 0$ range, and on the thickness D of each magnetic layer. Disregarding the potential presence of lines within walls or wall zigzagging effects which, obviously, cannot be included in a 2D description, intrinsic transitions from superimposed walls to parallel Néel walls or to saturation under the action of an in-plane hard-axis external field, h, have been successfully computed. For a given geometry (i.e. $[8/2/8]$ nm), a sketch of the phase diagram in the (h,J) space has been proposed. Special attention has been paid to the approach towards saturation, especially in the antiferromagnetic range. Generally speaking, strong intrinsic hysteresis effects should be expected.

References

[1] D.W. Donnet, J.N. Chapman, H. Van Kersteren and W. Zeper, J. Magn. Magn. Mater. 115 (1992) 342.

[2] L. Heyderman, H. Niedoba, H. Gupta and I.B. Puchalska, J. Magn. Magn. Mater. 96 (1991) 125.

[3] D.A. Herman Jr., B.E. Argyle, P.L. Trouilloud, B. Petek, L.T. Romankiw, P.C. Andricacos, S. Krongelb, D.L. Rath, D.F. Canaperi and M.L. Komsa, J. Appl. Phys. 63 (1988) 4036.

[4] M. Rührig, R. Schäfer, A. Hubert, R. Mosler, J.A. Wolf, S. Demokritov and P. Grünberg, Phys. Stat. Solidi (a) 125 (1991) 635.

[5] I. Tomáš, H. Niedoba, M. Rührig, G. Wittmann, A. Hubert, H.O. Gupta, L.J. Heyderman and I. Puchalska, Phys. Stat. Solidi (a) 128 (1991) 203.

[6] R. Kergoat, M. Labrune, J. Miltat, T. Valet and J.C. Jacquet, J. Magn. Magn. Mater. 121 (1993) 402.

[7] R. Kergoat, J. Miltat, T. Valet and R. Jérôme, J. Appl. Phys. 76 (1994) 7087.

[8] V. Grolier, J. Ferré, M. Galtier and M. Mulloy, J. Appl. Phys. 76 (1994) 6983 and references therein.

[9] A. Berger and H.P. Oepen, J. Magn. Magn. Mater. 121 (1993) 102 and references therein.

[10] R. Allenspach, J. Magn. Magn. Mater 129 (1994) 160 and references therein.

[11] D.T. Pierce, J.A.Stroscio, J. Unguris and R.J. Coletta, Phys. Rev. B49 (1994) 14564 and references therein.

[12] J.C. Slonczewski, B. Patek and B.E. Argyle, IEEE. Trans. Magn. 24 (1988) 2045.

[13] A. Yelon, in: Physics of Thin Films, eds. M.H. Francombe and R.W. Hoffman, Adv. Res. Dev., Academic Press, New York, 1971.

[14] S.S.P. Parkin, N. More, K.P. Roche, Phys. Rev. Lett. 64 (1990) 2304.

[15] P. Grünberg, S. Demokritov, A. Fuss, R. Schreiber, J.P. Wolf and S.T. Purcell, J. Magn. Magn. Mater. 104–107 (1992) 1734.

[16] P.F. Carcia, A.D. Meinhaldt and A. Suna, Appl. Phys. Lett. 47 (1985) 178.

[17] C.H. Lee, Hui He, F.J. Lamelas, W. Vavra, C. Uher and R. Clarke, Phys. Rev. B 42 (1990) 1066.

[18] A.E. LaBonte, J. Appl. Phys. 40 (1969) 2450.

[19] P. Trouilloud and J. Miltat, J. Magn. Magn. Mater. 66 (1987) 99.

[20] J. Miltat, A. Thiaville and P. Trouilloud, J. Magn. Magn. Mater. 82 (1989) 297.

[21] H. Rieder and A. Seeger, Phys. Stat. Solidi 46 (1971) 377.

[22] M. Labrune and J. Miltat, IEEE. Trans. Magn. 29 (1993) 2569.

[23] J. Miltat and M. Labrune, IEEE. Trans. Magn. 30 (1994) 4350.

[24] D.V. Berkov, K. Ramstöck and A. Hubert, Phys. Stat. Solidi (a) 137 (1993) 20.

[25] L. Néel, C. R. Acad. Sci. Paris 255 (1962) 1545, 1676.

[26] W.F. Brown Jr., in: Micromagnetics (Wiley, New York, 1963) (R.E. Krieger, Huntington, New York, 1978).

[27] J. Miltat, in: Applied Magnetism, eds. R. Gerber, C.D. Wright and G. Asti (Kluwer, Dordrecht, 1994), p.221.

[28] G.I. Rado and X. Weertman, J. Phys. Chem. Solids 11 (1959) 315.

[29] A. Hubert, in: Magnetic Domains (Springer-Verlag, Berlin, in press).

[30] A. Aharoni and J.P. Jakubovics, Phys. Rev. B43 (1991) 1290.

[31] D. Berkov, K. Ramstöck, T. Leibl and A. Hubert, IEEE Trans. Magn. 29 (1993) 2548.

[32] J.C. Slonczewski, IBM J. Res. Dev. 10 (1966) 377.

[33] M. Rührig and A. Hubert, J. Magn. Magn. Mater. 121 (1993) 330.

[34] M. Rührig, W. Rave and A. Hubert, J. Magn. Magn. Mater. 84 (1990) 102.

[35] J. Miltat and M. Labrune, Proc. IUMRS-ICPM Conf., Tokyo, 1993; see also M. Labrune and J. Miltat, J. Appl. Phys. 75 (1994) 2156.

[36] E.C. Stoner and E.P. Wohlfarth, Phil. Trans. R. Soc. A 204 (1948) 599.

[37] L. Heyderman, H. Niedoba, H. Gupta and I. Puchalska, J. Magn. Magn. Mater. 96 (1991) 125.

[38] E. Sannek, M. Rührig and A. Hubert, IEEE Trans. Magn. 29 (1993) 2500.

[39] H.O. Gupta, H. Niedoba, L.J. Heyderman, I. Tomáš, I. Puchalska and G. Sella, J. Appl. Phys. 69 (1991) 4529.

[40] L.J. Heyderman, Thesis, Bristol University 1991.